

# Problems of Position Reconstruction in Silicon Microstrip Detectors

Gregorio Landi\*

Dipartimento di Fisica e Astronomia, Universita' di Firenze and INFN, Sezione di Firenze,  
Largo E. Fermi 2 (Arcetri) 50125, Firenze, Italy

October 20, 2021 and August 11, 2005

## Abstract

The algorithms for position reconstruction in silicon micro-strip detectors are studied, and the signals of a minimum ionizing particle are simulated. The center-of-gravity distributions of the data events allow the fine tuning of the signal forms and of the strip response functions. In the sensors with floating strips the response function turns out to roughly approximate the response of a triangular function for the size of the signal involved. The simulations are extended to non orthogonal incidence. In these directions, and in general for all the asymmetric signal distributions, the standard application of the  $\eta$  algorithm introduces a systematic error. A signal reconstruction theorem gives the way to implement the corrections of this error.

**Keywords:** Center of gravity,  $\eta$ -algorithm, Position reconstructions, Silicon detectors.

## Contents

|          |  |          |
|----------|--|----------|
| <b>1</b> | <b>Introduction 2021</b>                     | <b>2</b> |
| <b>2</b> | <b>Introduction</b>                          | <b>3</b> |
| <b>3</b> | <b>The Signal Distribution</b>               | <b>4</b> |
| 3.1      | The Charge Diffusion . . . . .               | 4        |
| 3.2      | The Fourier Transform . . . . .              | 5        |
| 3.3      | Expressions for the COG and Energy . . . . . | 6        |
| 3.4      | The Reconstruction of $\varphi(x)$ . . . . . | 7        |
| <b>4</b> | <b>The Response Function</b>                 | <b>8</b> |
| 4.1      | Crosstalk . . . . .                          | 8        |
| 4.2      | Probability Distribution . . . . .           | 9        |
| 4.3      | The Data . . . . .                           | 9        |
| 4.4      | Position Reconstruction . . . . .            | 10       |

---

\*Corresponding author. Gregorio.Landi@fi.infn.it

|          |   |           |
|----------|---|-----------|
| <b>5</b> | <b>Simulations</b>  | <b>12</b> |
| 5.1      | Event Generation . . . . .  | 12        |
| 5.2      | Losses . . . . .  | 12        |
| 5.3      | Long Range Crosstalk . . . . .  | 12        |
| 5.4      | Data and Simulations . . . . .  | 13        |
| <b>6</b> | <b>Normal-strip side</b>  | <b>14</b> |
| 6.1      | The Response Function . . . . .                                       | 14        |
| 6.2      | Simulations . . . . .   | 15        |
| <b>7</b> | <b>Directions with <math>\theta \neq 0</math></b>                     | <b>15</b> |
| 7.1      | Simulations . . . . .   | 15        |
| 7.2      | Standard Deviations for the Reconstructions (Normal Strips) . . . . . | 16        |
| 7.3      | Distributions of $\varepsilon_{2,3} - \varepsilon$ . . . . .          | 17        |
| 7.4      | Error Due to $\varphi(x)$ Asymmetry . . . . .                         | 17        |
| 7.5      | The Complete $\varphi(x)$ -Reconstruction Theorem . . . . .           | 19        |
| 7.6      | Correction of the Systematic Error . . . . .                          | 21        |
| 7.7      | SD for the Floating Strip Side . . . . .                              | 22        |
| 7.8      | Distributions of $\varepsilon_{2,3} - \varepsilon$ . . . . .          | 23        |
| <b>8</b> | <b>Conclusions</b>  | <b>24</b> |

## 1 Introduction 2021

Position reconstructions for a special type of silicon micro-strip detectors were the argument of this work. This type of double-sided micro-strip detectors was developed for the ALEPH vertex detector, and installed also in the L3 micro-vertex detector. However, during our participation to the L3 experiment, our attention was attracted by the track reconstruction in the L3 central chambers using the spin glass theory. The definition of a spin, required the sole hit positions, thus, the properties of the signals produced by the micro-strip detectors were completely neglected. Also the developments of refs. [1, 2] were conceived principally for electromagnetic calorimeters, only marginally devoted the silicon trackers. However, the availability of a sample of test beam data of those double sided detectors (for the PAMELA experiment) raised our interest for an application of the methods of ref. [1]. Though, some new developments were necessary, the limitation of the  $\eta$ -algorithm to symmetric systems came in immediate evidence. The initial constant of the algorithm could be easily selected only in special cases (i.e. for orthogonal incidence without magnetic field). The recommendations of ref. [5], of an use for symmetric systems, was completely neglected in the implementation of the algorithm in data analysis of running experiments. The warning about this point probably originates few abandons of the  $\eta$ -algorithm in favor of the simpler center of gravity. Instead, a careful study of the simulations gave us an hint to demonstrate a first method of correcting this systematic error in absence of magnetic field.

The efficacy of the method was tested in a dedicated test beam (PoS(Vertex 2007) 048) with excellent results. Other more sophisticated methods were developed to correct the algorithm also for moderate magnetic fields. A better and simpler method was found as a by-product of an advanced method of track reconstruction. In fact, the observation of anomalies in the distributions of errors in some of the following scatter-plots (figure 11 for example) evidenced the impossibility of an identical variance for the hit errors (a standard assumption of all the books on mathematical statistics) and triggered a deep search

for realistic models of the error distributions of the observations. These realistic probabilities, turn out to be different for each hit. As expected for the Landau distribution of charge released. The realistic probabilities allowed substantial increases of the resolution for the track estimators. The developments, in the following, were essential for those advanced tasks, supported also by theorems that impose the account of the hit differences for optimal fits ([arXiv:2103.03464](https://arxiv.org/abs/2103.03464) and therein references).

The two-columns printing of Nuclear Instruments and Methods in Physics Research (A **554** 2005 226) introduced few typing errors, undetected by our proof revision, absent in this version.

## 2 Introduction

The aim of this work is an application of the developments of ref. [1] and [2] to the position reconstruction algorithms for silicon microstrip detectors. This application turns out somewhat complex and probably too detailed for the huge amount of data expected by future high energy experiments. But, in some experiments, the alignment parameters of the detector components are obtained through the position reconstruction algorithms. It is evident the need of maximum precision in these calibrations.

The detectors we are interested in are double sided silicon sensors of the type used in ALEPH [3] and L3 [4]: one side has all the strips connected to the electronics, the other side has one strip each two connected to the electronics. The unconnected strips are called "floating strips".

The first step is the simulation of the signals released in the sensor by a minimum ionizing particle (MIP). Our simulations are intended to be realistic enough to allow a non trivial exploration of the position reconstruction properties for non orthogonal incidences of a MIP. The fact that the strip charge collection works as a powerful low pass filter assures that few parameters are really important. To select them, we will use in reverse mode the properties of the position reconstruction algorithms.

We proved in ref. [1] the strict connection of the center of gravity (COG) algorithm with the Fourier Transform (FT) of the signal collected. Thus, our first task will be the calculation of the charge distribution (and its FT) that arrives to the collecting electrodes. The signal shapes we will explore are average signals; the fluctuations of the energy release and of its diffusion are different in each event, but their averages are supposed well defined. Section 2 is devoted to the determination of the FT of the signals integrated by the strips. A parameter is left free and extracted from the data

In the sections 3 and 4, the experimental data are used to define the strip response function and a form factor of the signals. The data are obtained from a test beam of the PAMELA tracker [9], the sensors are double sided and the particle incidence is orthogonal. The strip property is contained in a single function, the response function. In a rudimentary form the strip response function integrates the energy released in its range. The crosstalk (and the loss) modifies this picture and the best form must be extracted from the data. For the floating strip detectors the crosstalk is fundamental and the response function model must be well tuned to produce faithful simulations. In this application we will prove the effectiveness of signal reconstruction theorems that are contained in the COG properties.

Section 5 deals with the simulation of a normal strip detector, here the crosstalk is small, but its effect is well seen in the data.

In section 6 the simulations are extrapolated to non orthogonal incidence of the MIP. We will see that the asymmetry of the signal distribution introduces a systematic error in the standard application of the  $\eta$ -algorithm [5]. A method is defined to correct this error, the corrections are derived from a generalization of a reconstruction theorem to asymmetric signals.

### 3 The Signal Distribution

#### 3.1 The Charge Diffusion

Our task is the simulation of the signals produced by a MIP crossing a 300  $\mu\text{m}$  silicon sensor. In the absence of magnetic field and neglecting  $\delta$ -ray production and multiple scattering, the MIP releases the initial ionization along a linear path. The electric field in the interior of the detector drifts the charges

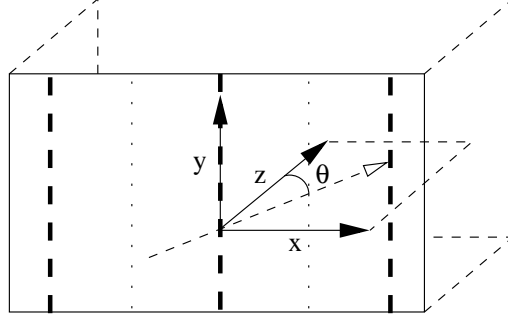


Figure 1: Reference system on the sensor, the three dashed thick lines are the collecting electrodes, the thin dashed arrow is the direction of an incoming particle forming an angle  $\theta$  with the  $z$ -axis

toward the corresponding electrode. During the drift, the charge diffusion modifies the form of the initial ionization.

The initial charge distribution (of both signs) is expressed as in ref. [1]:

$$\varphi_0(\mathbf{r}, \mathbf{r}_0, \mathbf{L}) = \int_0^1 d\lambda \delta(\mathbf{r} - \mathbf{r}_0 - \mathbf{L}\lambda) \quad (1)$$

where  $\delta(\mathbf{r}) = \delta(x)\delta(y)\delta(z)$ .  $\varphi_0(\mathbf{r}, \mathbf{r}_0, \mathbf{L})$  is a function of  $\mathbf{r}$  defined on  $\mathbb{R}^3$ , it describes a uniform charge distribution along the vector  $\mathbf{L}$  and impact point  $\mathbf{r}_0$ . The impact point is on the detector surface and the ionization path  $\mathbf{L} \equiv \{L_x, L_y, L_z\}$  is contained in the detector interior. If  $L_0$  is the detector thickness, we have  $L_z = L_0$ .

The diffusion process transforms an initial Dirac- $\delta$  charge distribution in a gaussian of half width proportional to the drift time. The final charge distribution, arriving to the collecting electrodes, has the form:

$$\varphi(\mathbf{r}_0, \mathbf{r}_f, \mathbf{L}) = \int_{\mathbb{R}^3} d^3\mathbf{r}' \varphi_0(\mathbf{r}', \mathbf{r}_0, \mathbf{L}) g(\mathbf{r}' - \mathbf{r}_f) \quad (2)$$

where  $\mathbf{r}_f = \{\mathbf{x}, z_f\}$  and  $\mathbf{x} \equiv \{x, y\}$ ,  $\mathbf{x}$  is defined on  $\mathbb{R}^2$  and  $z_f$  is the plane of the collecting electrode,  $g(\mathbf{r})$  accounts the diffusion process. The reference system is illustrated in figure 1, it has the origin in the plane of the collecting electrodes, the  $z$ -axis is perpendicular to that plane and directed toward the sensor interior. The  $x$ -axis is perpendicular to the strip direction. For both charge we will put the impact point at  $z = 0$  and  $z_f = z_0 = 0$  (in one case the impact point is in reality an outgoing point).

The diffusion gives to  $g(\mathbf{r})$  the form:

$$g(\mathbf{x}, t) = \frac{1}{(\sqrt{2\pi}\sigma(t))} \exp\left[-\frac{\mathbf{x}^2}{2\sigma(t)^2}\right]. \quad (3)$$

$\sigma(t)$  is a function of the diffusion process and depends from the time  $t$  spent by the charges in their drift from the production point to  $z = 0$ :

$$\sigma(t) = \sqrt{\mu D t} \quad (4)$$

where  $D$  is proportional to the absolute temperature. The time  $t$  is connected to the electric field in the semiconductor interior and to the charge mobility. To simplify we will take a constant electric field  $E$  in  $z$  direction, and its effective value will be extracted from the data. For  $t(z)$  and  $\sigma$  we have ( $z = \lambda L_0$ ):

$$t(\lambda) = \frac{\lambda L_0}{\mu E} \quad \sigma^2 = \frac{DL_0\lambda}{E} = \alpha\lambda \quad \alpha = \frac{DL_0}{E} \quad (5)$$

More realistic field configuration could be used (with an increase of the unknowns), but this refinement is irrelevant for the simulation.

From equations 2 and 3, and recalling our position  $z_0 = z_f$ ,  $\varphi(\mathbf{r}_0, \mathbf{r}_f, \mathbf{L})$  does not depend on  $z_0$  and  $z_f$ , and it becomes:

$$\varphi(\mathbf{x}_0, \mathbf{x}, \mathbf{L}) = \int_0^1 d\lambda \frac{1}{(\sqrt{2\pi\alpha\lambda})} \exp\left[-\frac{(\mathbf{x} - \mathbf{x}_0 - \mathbf{L}_x\lambda)^2}{2\alpha\lambda}\right] \quad (6)$$

where we pose  $\mathbf{L}_x \equiv \{L_x, L_y\}$ .

### 3.2 The Fourier Transform

The equations of ref. [1, 2] are expressed with the FT of the charge distribution respect to  $\{\mathbf{x}\}$ . Defining  $\Phi(\mathbf{x}_0, \mathbf{L}_x, \omega)$  the FT of  $\varphi(\mathbf{x}_0, \mathbf{x}, \mathbf{L})$ , its expression is:

$$\begin{aligned} \Phi(\mathbf{x}_0, \mathbf{L}_x, \omega) &= \int_{\mathbb{R}^2} \frac{d\mathbf{x}}{(2\pi)^2} \rho_f(\mathbf{x}_0, \mathbf{L}_x, \mathbf{x}) e^{-i\omega \cdot \mathbf{x}} \\ &= \int_0^1 d\lambda \int_{\mathbb{R}^2} e^{-i\omega \cdot \mathbf{x}} \frac{1}{\sqrt{2\pi\alpha\lambda}} \exp\left[-\frac{(\mathbf{x} - \mathbf{x}_0 - \mathbf{L}_x\lambda)^2}{2\alpha\lambda}\right] d\mathbf{x} \\ &= \int_0^1 d\lambda e^{-i(\mathbf{x}_0 + \mathbf{L}_x\lambda) \cdot \omega} e^{-\alpha\lambda\omega^2/2} \end{aligned} \quad (7)$$

where we pose  $\omega = \{\omega_x, \omega_y\}$ . The integration on  $\lambda$  gives:

$$\Phi(\mathbf{x}_0, \mathbf{L}_x, \omega) = e^{-i\mathbf{x}_0 \cdot \omega} \frac{1 - e^{-i\mathbf{L}_x \cdot \omega} e^{-\alpha\omega^2/2}}{i\mathbf{L}_x \cdot \omega + \alpha\omega^2/2} \quad (8)$$

The parameter  $\alpha$  collects important properties of the detector; temperature, thickness and the effective constant field  $E$ . The values of  $\alpha$  for the two sensor sides will be extracted from the data.

The equation (8) allows asymmetric forms for the signal distributions easy to manage even for pixel detectors.

In our equations  $\Phi(\mathbf{x}_0, \mathbf{L}_x, \omega)$  has the COG in the origin of the reference system, this gives the relation:

$$\lim_{\omega \rightarrow 0} \frac{\partial \Phi(\mathbf{x}_0, \mathbf{L}_x, \omega)}{\partial \omega} = -\frac{1}{2}i(\mathbf{L}_x + 2\mathbf{x}_0) = 0.$$

In the plane  $z = 0$ , the impact point  $\mathbf{x}_0$  is related to the to the initial ionization segment  $\mathbf{L}_x$  by:

$$\mathbf{x}_0 = -\frac{\mathbf{L}_x}{2}$$

and it has the same expression as in the absence of diffusion ( $\alpha = 0$ ). We will need impact points uniformly distributed on a strip and, for the above equation, even their COG's. The FT shift theorem [6] allows to move the COG where needed.

In the following, we will limit our study to inclined tracks with  $L_x \neq 0$  and  $L_y = 0$ .

The equation (8) can be rearranged in:

$$\Phi(\mathbf{L}_x, \omega) = e^{-\alpha\omega^2/4} \frac{\sin(\frac{1}{2}\mathbf{L}_x \cdot \omega - i\frac{1}{4}\alpha\omega^2)}{(\frac{1}{2}\mathbf{L}_x \cdot \omega - i\frac{1}{4}\alpha\omega^2)}. \quad (9)$$

This form is an evident generalization of a track energy introduced in ref. [1]. A microstrip sensor integrates on  $y$  the signal distribution  $\varphi(\mathbf{x}, \mathbf{L}_x)$ , and in equation 9 we have  $\omega_y = 0$ . The surviving  $\omega_x$  variable will be indicated with  $\omega$ , and  $\varphi(x)$  the integrated signal distribution. Figure 2 illustrates  $\varphi(x)$  at various incidence angles ( $L_x = \tan(\theta)$ ). The COG of each  $\varphi(x, \theta)$  is in the origin  $x = 0$ .

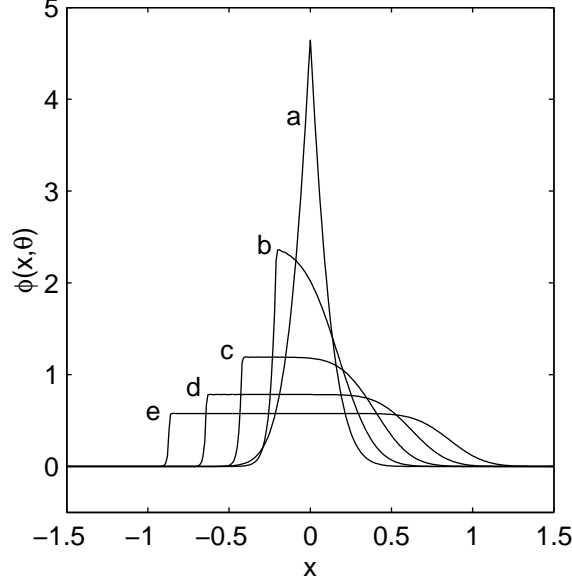


Figure 2: Form of the signal distribution at various incidence angles. The curves a, b, c, d ed e are respectively for  $\theta = 0^\circ$ ,  $\theta = 5^\circ$ ,  $\theta = 10^\circ$ ,  $\theta = 15^\circ$  and  $\theta = 20^\circ$

### 3.3 Expressions for the COG and Energy

The asymmetric signal distributions require a slight generalization of the equations in ref. [1], where symmetric signals were assumed. The equations of the COG-algorithms with two and three strips will be considered. As in ref. [1] we indicate with  $S_\varepsilon(\omega)$  the FT of the sampled convolution of the signal (transformed in a periodic signal with a period  $T \gg \tau$ ) with the strip response. The derivative of  $S_\varepsilon(\omega)$  respect to  $\omega$  (normalized with  $S_\varepsilon(0)$ ) is the COG position of the signals collected by the strips. The parameter  $\varepsilon$  is the COG position of the initial signal distribution, and the shift theorem of FT introduces its functional dependence in the equations:

$$S_\varepsilon(\omega) = \sum_{n=-\infty}^{+\infty} \Phi_n^p P\left(\frac{2n\pi}{T}\right) \exp\left(\frac{-i2n\pi\varepsilon}{T}\right) H\left(\omega - \frac{2n\pi}{T}\right). \quad (10)$$

In equation 10,  $P(2n\pi/T)$  is the FT of the strip response function  $p(x)$ , and it will be determined in the following.  $\Phi_n^p$  is equation 9 for  $\omega = 2\pi n/T$  as imposed by periodicity:

$$\Phi_n^p = \frac{1}{T} \Phi\left(L_x, \frac{2\pi n}{T}\right). \quad (11)$$

$H(\omega)$  is a function of the strip number used in the algorithm. In the case of two strips it is ( $\tau$  is the strip dimension) :

$$\begin{aligned} H(\omega) &= 1 + e^{(-i\omega\tau)} & \varepsilon > 0 \\ H(\omega) &= 1 + e^{(+i\omega\tau)} & \varepsilon < 0 \end{aligned}$$

and for three strips:

$$H(\omega) = 1 + 2 \cos(\omega\tau)$$

Due to the normalization of  $\varphi(x)$  and  $p(x)$ ,  $S_\varepsilon(0)$  is the signal collection efficiency of the algorithm. The efficiency for the three-strip algorithm is given by:

$$S_\varepsilon(0) = \frac{3 P(0)}{T} + 2 \sum_{n=1}^{+\infty} P\left(\frac{2n\pi}{T}\right) \left[1 + 2 \cos\left(\frac{2n\pi\tau}{T}\right)\right] \text{Real}\left[\Phi_n^p \exp\left(-i\frac{2n\pi\varepsilon}{T}\right)\right] \quad (12)$$

and the three-strip COG is:

$$x_{g3} = \frac{-4\tau}{S_\varepsilon(0)} \sum_{n=1}^{+\infty} P\left(\frac{2n\pi}{T}\right) \sin\left(\frac{2n\pi\tau}{T}\right) \text{Imag}\left[\Phi_n^p \exp\left(-i\frac{2n\pi\varepsilon}{T}\right)\right] \quad (13)$$

If in equation 10 we substitute  $H(\omega) = \exp(-i\omega l\tau)$  of a single strip at  $l\tau$ , the expression of  $S_\varepsilon(\omega)$  for  $\omega \rightarrow 0$  gives the fraction of the energy collected by the  $l$ -th strip:

$$E_\varepsilon^l = \sum_{n=-\infty}^{+\infty} \Phi_n^p P\left(\frac{2\pi n}{T}\right) \exp\left[-i\frac{2\pi n}{T}(\varepsilon - l\tau)\right]. \quad (14)$$

Equation 14 is another way to write the convolution of  $\varphi(x - \varepsilon)$  with  $p(x)$  for a strip. The periodicity imposed to  $\varphi(x)$  allows to write the convolution as Fourier Series (FS) with all the benefits to use a fast converging discrete sum in place of an integral. So, for the three strip COG  $x_{g3}$ , we can use equation 13 or use  $x_{g3} = (E_\varepsilon^1 - E_\varepsilon^{-1}) / (E_\varepsilon^1 + E_\varepsilon^0 + E_\varepsilon^{-1})$ . The last one will be preferred to be consistent with the simulations.

### 3.4 The Reconstruction of $\varphi(x)$

Equation 14 requires further information that we have to extract from the data; a reasonable form of the strip response function  $p(x)$  (with FT  $P(2n\pi/T)$ ) and the best value of  $\alpha$  of equation 9. These sensor properties are bound together and we must fix their better combination with successive tests. We have some relations to use for this task. The relation, proved in ref [1], of  $dx_g(\varepsilon)/d\varepsilon$  with  $\varphi(x)$  can be used as a starting point. In that case the response function was an interval function ( $\Pi(x) = 1$  for  $|x| < 1/2$  and zero elsewhere). For  $dx_g(\varepsilon)/d\varepsilon$  we have ( $\Phi(\omega)$  FT of  $\varphi(x)$ ):

$$\frac{dx_g}{d\varepsilon} = 1 + \sum_{k=1}^{+\infty} (-1)^k \text{real}\left[\exp\left(\frac{2k\pi\varepsilon}{\tau}\right) \Phi\left(-\frac{2k\pi}{\tau}\right)\right]$$

which for Poisson identity [7] can be reassembled into (with  $\Phi(0) = 1$ ):

$$\frac{dx_g}{d\varepsilon} = \sum_{k=-\infty}^{+\infty} \exp\left[i\frac{2k\pi}{\tau}\left(\varepsilon - \frac{\tau}{2}\right)\right] \Phi\left(-\frac{2k\pi}{\tau}\right) = \tau \sum_{L=-\infty}^{+\infty} \varphi\left(-\varepsilon + \frac{\tau}{2} - L\tau\right). \quad (15)$$

If the support of  $\varphi(x)$  is  $\leq \tau$ , the multiplication of equation 15 by  $\Pi(-x/\tau + 1/2)$  reconstructs exactly the function  $\varphi(-x + \tau/2)$ . It is easy to extract from the reconstruction theorem 15 a relation of peaks in the COG probability distribution and discontinuities in the response function. In regular detector and a  $\varphi(x)$  for  $\theta = 0$ , one has a peak in the COG probability distribution and a discontinuity in  $p(x)$  at the strip border. In a detector with floating strip the COG probability has three peaks, and we can guess that other discontinuities are present in the response function.

## 4 The Response Function

### 4.1 Crosstalk

The set of candidate response function  $p(x)$  will be selected among the ones defined in [1] as uniform crosstalk, i.e. response function with its influence extending outside the range of a strip and conserving the energy (in the case of an infinite sampling). A sufficient condition for the uniform crosstalk is to have arbitrary functions (even Dirac  $\delta$ -function) convoluted with an interval function of size  $\tau$ . In the following we will work with  $\tau = 1$ .

This  $p(x)$  is suitable to simulate the effect of a floating strip:

$$p(x) = \int_{-\infty}^{+\infty} \Pi(x-x') \{ a_1 [\delta(x' - 1/4) + \delta(x' + 1/4)] + a_2 [\delta(x' - 1/2) + \delta(x' + 1/2)] \} \quad (16)$$

It is easy to show that the  $p(x)$  of figure 3 produces the three typical peaks of the  $\eta$  distribution [5]

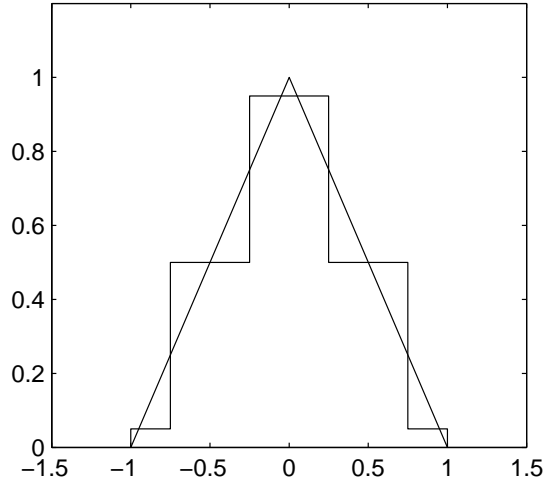


Figure 3: Response function of equation 16 with  $a_1 = 0.45$  and  $a_2 = 0.05$ , a type of uniform crosstalk that reproduces the lateral peaks around  $x_g = \pm 1/2$ . The triangular response function (with base 2) is reported for comparison

( $\eta = E_L/(E_L + E_R)$  where  $E_L$  and  $E_R$  are the left and right strips of the two largest signal couples) of a floating strip sensor. In fact, figure 3 can be read as the plot of the possible energies collected by the strips in the case of a Dirac  $\delta$  signal. The ordinate of each strip center in the array are just the energies collected by an event. Given the strip pitch  $\tau = 1$ , the sample of events is generated by moving the strip array to cover a strip interval. Two possible combination of energy are allowed: equal energies or 0.9 and 0.05. The ratio of one of this pair of energies divided by the sum of the two, gives three  $\delta$ -like peaks at the positions 0.054, 0.5, 0.94 and relative intensity (1 2 1). A smearing of the response function with a realistic signal distribution and further fine tuning is able to reproduce the experimental distributions.

The results of an experiment with an infrared laser on a double sided silicon sensor [8] show an energy collection similar to figure 3. In their figure 6 a step-like plot is easily recognized. The due differences must be kept in mind; the laser beam is not a Dirac  $\delta$ -function, the strip metallization is opaque to the laser beam.

The response function of equation 16 with  $a_1 = 0.5$  and  $a_2 = 0$  and  $\Phi(\omega)$  FT of  $\varphi(x)$  gives for the



COG (infinite sampling) the equation:

$$x_g(\varepsilon) = \varepsilon - i \sum_{m \neq 0, m=-\infty}^{+\infty} \frac{(-1)^m}{4m\pi} \Phi(-4\pi m) e^{i4\pi m \varepsilon} \quad (17)$$

Deriving in  $\varepsilon$ , the Poisson identity gives:

$$\frac{dx_g}{d\varepsilon} = \frac{1}{2} \sum_{l=-\infty}^{+\infty} \varphi(-\varepsilon + \frac{1}{4} - \frac{l}{2}) \quad (18)$$

The equation 18 is a sum of infinite copies of  $\varphi(x)$  centered at  $1/4$  and  $3/4$  of each strip. It will be used as a guide to select a response function  $p(x)$  for the simulations.

## 4.2 Probability Distribution

As we discussed in ref. [1], given an identical signal distribution for each event, the probability  $\Gamma(x_g)$  to have  $x_g$  ( for each algorithm) is the product of the probability  $P(\varepsilon)$  to have  $\varepsilon$  and  $|d\varepsilon(x_g)/dx_g|$ :

$$\Gamma(x_g) = P(\varepsilon) \left| \frac{d\varepsilon(x_g)}{dx_g} \right| \quad (19)$$

This equation could be handled as a differential equation, if we prove that the unknown function has always the same sign. We showed in [1] that  $d\varepsilon/dx_g$  is non negative for a large set of signal distribution and algorithms with different number of strips. For an infinite sampling, equations 15 and 18 show immediately that  $dx_g/d\varepsilon$  is always non negative if  $\varphi(\varepsilon)$  is non negative.

In real events, the conditions giving equation 19 are always violated. The noise is present, the charge deposition fluctuates, different strips are hit in different events, and we never have a single  $\varepsilon(x_g)$ . The experimental probability distribution is an average over different type of signals produced by the particles and of responses of different strips of the detector. Being the probability an average over fluctuations, also the reconstruction will be an average, and it will be effective if the fluctuations and the noise is not too high. With these limitations in mind and for a constant  $P(\varepsilon)$ , the equation (19) is easy to solve given an initial condition:

$$\varepsilon(x_g) = \tau \int_{x_g^0}^{x_g} \Gamma(y) dy + \varepsilon(x_g^0). \quad (20)$$

The selection of the initial condition  $\varepsilon(x_g^0)$  is a critical point, we will see in the following, for  $\theta \neq 0$ , the amplitude of the systematic error given by the error on  $\varepsilon(x_g^0)$ .

To simplify, the symmetry of the strip response  $p(x)$  will be assumed. So, for symmetric  $\varphi(x)$ , two points have the property  $x_g(\varepsilon) = \varepsilon$ :  $x_g(\pm 1/2) = \pm 1/2$  and  $x_g(0) = 0$ . In this case the initial condition is exactly defined.

## 4.3 The Data

To fine tuning our simulation, we need a comparison with experimental data. The data used are obtained from a test beam of a tracker prototype for the PAMELA [9] experiment.

The beam particles are  $\pi^+$  and the incidence angle is orthogonal to the plane of the sensors. Each sensor is  $300 \mu\text{m}$  thick silicon wafer where the junction side and the ohmic side are arranged to position measurements. In the junction side  $p^+$  strips are implanted and one of two connected to the read out electronics (pitch  $50 \mu\text{m}$ ). The ohmic side has  $n^+$  strips orthogonal to the strips of the junction side and each  $n^+$  strips connected to the read out electronics (pitch  $67 \mu\text{m}$ ). No magnetic field is present.

The sign of the read-out signals is arranged to be independent from the collected charge. The events are selected in a standard way and, after pedestal and common noise subtraction, they are assembled

with the data of the maximum-signal strip at the center of an eleven component vector. The other vector components contain the data of the neighboring strips. The pedestal and common noise subtraction attenuates almost completely the ADC quantization.

Low signal values of any sign, contained in the data, are used in the algorithms. No attention is given to the cluster size. We select the events to have the sum of the collected signal in the maximum strip and in its two adjacent greater than 40 ADC counts and lower than 350 ADC counts. In this range of ADC counts the Landau peak is fully contained. We cut the high energy tail where it is probable to have  $\delta$ -rays or other reactions, and the low energy tail for its low signal to noise ratio.

The far strip signals are use to estimate the noise and the crosstalk.

The COG algorithms have the origin of their reference system in the center of the strip with the maximum signal. (In section 6 we will abandon this convention and the true position will be considered)

We indicate with  $x_{gn}$  the COG calculated with  $n$  strips. The two strip algorithm  $x_{g2}$  has the best signal to noise ratio, but, due to the crosstalk has an appreciable discontinuity in the origin even with  $\theta = 0$  and regular strips. The noise strongly attenuates the discontinuity, but a drop around  $x_{g2} \approx 0$  is evident in the probability distribution.

The  $x_{g3}$  algorithm tends to have two region of low probability at the strip borders.

The infinite sampling is excluded for the noise, thus we can expect some deviation in the  $\varphi(\varepsilon)$  reconstructed with  $\varepsilon$  extracted from  $x_{g2}$  and  $x_{g3}$ . These deviations are well localized and we expect that  $x_{g2}$  and  $x_{g3}$  are interesting reconstruction tools outside the regions of strong deviations.

#### 4.4 Position Reconstruction

In the  $x_{g2}$  algorithm, we use maximum-signal strip and the maximum (of any sign) between the two lateral. In the  $x_{g3}$  we use the maximum-signal strip and the two lateral.

We assume that the probability  $P(\varepsilon)$  is constant on a strip length after the subtraction of the maximum integer contained in  $\varepsilon$ , and the noise does not destroy the validity of equation 20. The histograms of  $\Gamma(x_{g2})$  and  $\Gamma(x_{g3})$  are inserted in equation 20, and  $\varepsilon_2(x_{g2})$  and  $\varepsilon_3(x_{g3})$  are obtained with a numerical integration. The initial condition  $\varepsilon_{2,3}(-1/2) = -1/2$  is used. Due to the noise  $\varepsilon_{2,3}(x_{g2,3})$  are an estimate of the most probable  $\varepsilon$  given  $x_{g2,3}$ . Where  $\varepsilon_{2,3}$  or  $x_{g2,3}$  indicate simultaneously  $\varepsilon_2$  and  $\varepsilon_3$  or  $x_{g2}$  and  $x_{g3}$ .

The numerical forms of  $\varepsilon_{2,3}(x_{g2,3})$  are not practical for the successive uses, it is fundamental to have analytical expressions. The natural way to construct analytical expressions is to consider the periodicity of  $\varepsilon(x_g)$  in presence of a true uniform illumination. This is not our case, but we have to near this condition. Our set of data are scattered on a large set of strips, and it is improbable to have the same strip few times. In the algorithm, we collect together all the signal on a single strip to generate a fictitious uniform illumination on that strip, all the other strips have no illumination. But, due to the uniformity of the strip properties, we can consider all the strips with an identical incident illumination and an identical probability  $\Gamma(x_g)$ , this virtual total probability becomes periodical:

$$\Gamma^p(x_g) = \sum_{j=-\infty}^{\infty} \Gamma(x_g + j).$$

With  $\Gamma^p(x_g)$ , the Fourier series (FS) is the natural way to fit the function  $\varepsilon_n - x_{gn}$  that is itself periodic:

$$\begin{aligned} \varepsilon_n(x_{gn}) - x_{gn} &= \sum_{k=-\infty}^{+\infty} \alpha_k e^{i2\pi k x_{gn}} \\ x_{gn}(\varepsilon_n) - \varepsilon_n &= \sum_{k=-\infty}^{+\infty} \beta_k e^{i2\pi k \varepsilon_n} \end{aligned} \tag{21}$$

The periodicity of  $\Gamma^p(x_{gn})$  is a method to handle the events with  $|x_{gn}| > 1/2$ . In the  $x_{g2}$ -algorithm, it is very improbable to have  $|x_{g2}| > 1/2$ . The less energetic strip must have a large negative value with its

modulus greater than  $2/3$  the energy of the other strip, and this never happens in our data. In the  $x_{g3}$  algorithm, events with  $|x_{g3}| > 1/2$  are possible, and in the  $x_{g4}$  algorithm an important fraction of events has  $|x_{g4}| > 1/2$ .

Given our interest in  $\varepsilon_n(x_{gn})$ , we use the first of the equations 21 with a reduced number of terms ( $\alpha_k = 0$  for  $|k| \geq 15$ ) to filter the high frequencies of the numerical integration on a small bin-size histogram. The  $\alpha_k$  are obtained with another numerical integration with the standard form of the FS coefficients.

Dropping the number of strips in the notation, the derivative  $dx_g(\varepsilon)/d\varepsilon$  is given by the identity:

$$\frac{dx_g(\varepsilon)}{d\varepsilon} = \frac{1}{\frac{d\varepsilon(x_g)}{dx_g}} = [1 + \sum_{k=-\infty}^{+\infty} (i2\pi k)\alpha_k e^{i2\pi k x_g}]^{-1}. \quad (22)$$

and the plot of the reconstructed  $\varphi(\varepsilon)$  is generated with  $\varepsilon(x_g)$  on the  $x$ -axis, and the  $x_g$ -function of equation 22 on the  $y$ -axis. This method is very effective, as we can see in figure 4. Here the  $x_{g3}$  from data and from the simulations are elaborated in the same way. From equation 18 we expect two copies of  $\varphi(\varepsilon_3)$  centered at  $\pm 0.25$ . The similarity of the two reconstructed  $\varphi(\varepsilon_3)$  is noticeable and they are near to the noiseless  $dx_{g3}(\varepsilon)/d\varepsilon$  (obtained deriving the equation 13). The parameter  $\alpha = 0.0324$  is used in the simulations. The details of the simulations will be given in the coming section, here we test the response function and the diffusion parameter  $\alpha$ .

The two lateral increases are typical of the  $x_{g3}$ -algorithm. In the noiseless case, two discontinuities are present in  $x_{g3}(\varepsilon_3)$  at  $\varepsilon_3 = \pm 1/2$ . The noise smooths the discontinuities in regions of fast variation that give a substantial increases to the derivative. The noiseless  $x_{g3}(\varepsilon)$  and its derivative (given by the equation 13) are defined in the interior of a single strip and the two Dirac  $\delta$  are outside the definition domain.

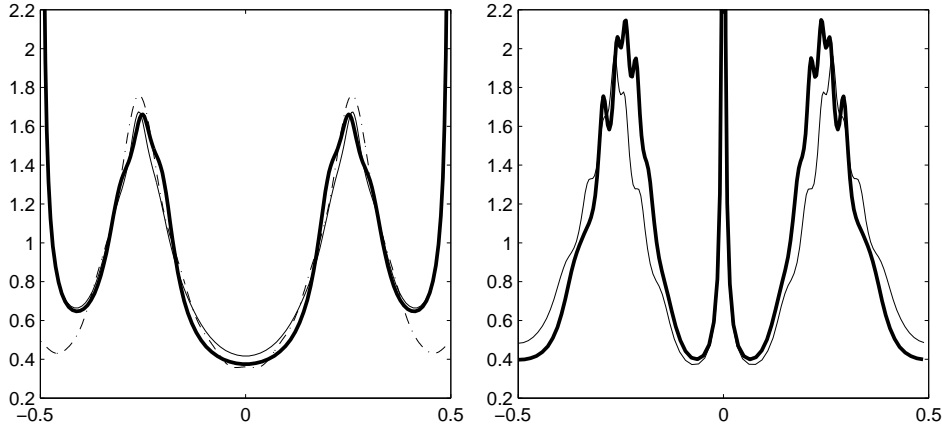


Figure 4: To the left  $\varphi(\varepsilon)$  obtained by the  $x_{g3}$  algorithm applied to the data (thick line), given by the simulations (thin line), and deriving equation 13 (dash-dot line). To the right the algorithm is  $x_{g2}$ , the thick line is given by the data, the thin line by the simulations.

To see the effect of limited sampling, in the left side of figure 4 the equation 22 is applied to  $\varepsilon_2(x_{g2})$  given by the data and by the simulations. Even here the two reconstructions are similar, and similar is the number of oscillations, these are given by the lower number of events respect to the regions with  $\varepsilon \approx 0$  and  $\varepsilon \approx \pm 1/2$ . The large increase for  $\varepsilon = 0$  is typical of  $x_{g2}$  that has there a discontinuity in the absence of noise.

The result of equation 18 is reported in figure 5 with all the reconstructions of figure 4.

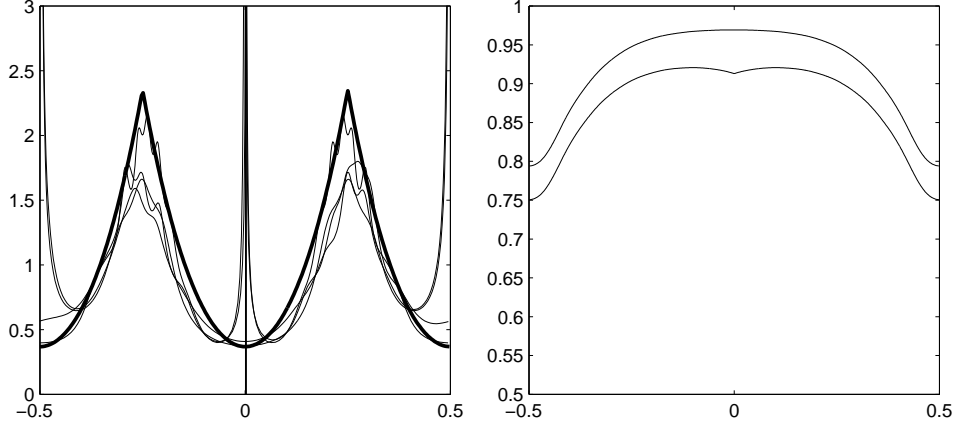


Figure 5: The thick line is  $\varphi(\varepsilon)$  as given by equation 18, the thin lines are the other reconstructions of figures 4. To the right, the efficiency of  $x_{g_3}$  (higher curve) and of  $x_{g_2}$  (lower curve). The signal loss is visible as the drop around  $\pm 0.5$ .

## 5 Simulations

### 5.1 Event Generation

To generate the events, we use the following procedure. A set of random points  $\{\varepsilon_i\}$  is generated with an uniform distribution on 3 strips. The points  $\varepsilon_i$  are used to calculate the fraction of energy  $E_{\varepsilon_i}^l$  (equation 14) for five strips  $\{l\}$  centered around the strip containing  $\varepsilon_i$ . For each event, a random number is extracted with the distribution of the total experimental charge (in ADC counts) collected by three strips (the one with the maximum signal and the two adjacent). All the  $E_{\varepsilon_i}^l$  of the event  $i$  are scaled with this random factor. The noise is added to each strip with a gaussian distribution modelled from the data.

### 5.2 Losses

Further details must be defined to fine tuning our simulations to the data. From the beginning, we suppose that the signal shape is the same at least on average. The noise and the fluctuations of the primary ionization modify the pattern of the collected energy for each events, but the  $x_g$ -histograms must not change. On the contrary, the  $x_g$ -histograms for events with energy less than the Landau maximum (175 ADC counts for our data) have a larger probability for  $|x_g| \approx 1/2$  than the events with higher energies. An easy explanation of these differences can be a signal loss in the detector interior around the floating strip.

We can simulate this loss with an efficiency reduction around the strip borders. Cutting two grooves around  $x = \pm 1/2$  on  $p(x)$ , one obtains the efficiency plots of figure 5. The efficiency drop around  $x = \pm 0.5$  is exclusively given by the loss. This type of loss is qualitatively similar to that measured in ref [10]; in our case it is guessed by the  $x_{g_{2,3}}$ -probability plots for events with different total energy.

### 5.3 Long Range Crosstalk

In section 4.1 we discussed the main crosstalk produced by the floating strip. But, in the strips adjacent to that used in  $x_{g_3}$ , we see an average shift of the collected signals toward the maximum signal strip. This means that a long range crosstalk is present in the data. To produce detailed simulations, other terms must be added to  $p(x)$  with tails longer than that of figure 3. In figure 6, the effect of the crosstalk

(and the quality of the simulations) is clearly seen. Here  $\varepsilon_3(x_{g3}(j))$  vs  $\varepsilon_2(x_{g2}(j))$  for data events and for simulated events can be compared, it is evident a strict similarity of the distribution patterns. The total elimination of all the crosstalk drastically modifies the scatter plot as can be see in the plots of figure 9.

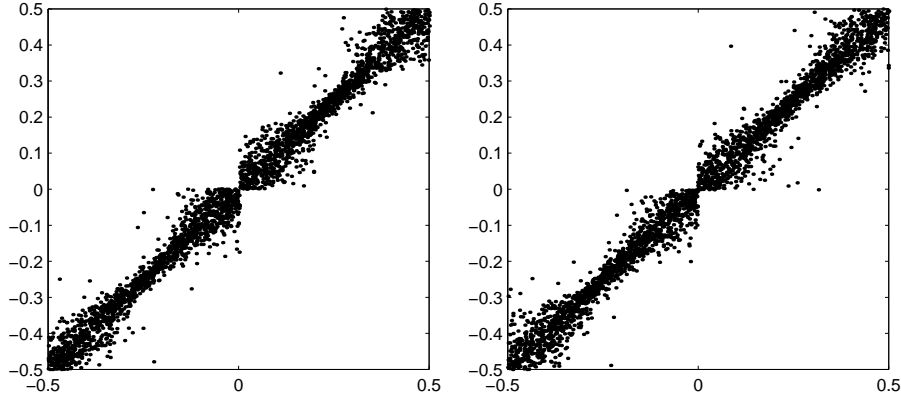


Figure 6: Samples of  $\{\varepsilon_3(x_{g3}(j)), \varepsilon_2(x_{g2}(j))\}$ . To the left the data. To the right the simulations. Identical forbidden regions are present in the two scatter plots.

#### 5.4 Data and Simulations

The consistency of the simulations with the data can be appreciated in figure 7. Here the probability distributions of  $\Gamma^p x_{g3}$  are compared. The two curves are obtained from equation 21, but this time we plot  $d\varepsilon(x_{g3})/dx_{g3}$  versus  $x_{g3}$ . This is apparently a trivial operation, first  $\Gamma^p(x_{g3})$  is integrated and after it is derived to return to  $\Gamma^p(x_{g3})$ . In reality this procedure applies a consistent low pass filter to  $\Gamma^p(x_{g3})$ .

Figure 8 reports a sample of simulated  $x_{g2}$  and  $x_{g3}$  values. The two overlapping lines are  $x_{g2}(\varepsilon_2)$  obtained from simulated events with noise and the noiseless  $x_{g2}(\varepsilon)$ . If we exclude a smoothing in the rapid variation regions (around  $x_{g2} = 0$ ), the overlap is almost complete. The noise works as a low pass filter. Similar overlap is observed even for the noisy  $x_{g3}(\varepsilon_3)$  with the plot of noiseless  $x_{g3}(\varepsilon)$ . In spite of these overlaps, the error  $\varepsilon_{2,3}(x_{g2,3}) - \varepsilon$  remains appreciable. In fact, the reconstruction algorithm  $\varepsilon_{2,3}(x_{g2,3})$  explores the scatter-plot of figure 8 along the horizontal line going through  $x_{g2,3}$ . The noise shifts  $x_{g2,3}$  along a vertical line passing through the noiseless  $x_{g2,3}(\varepsilon)$ . If the shift is large and/or the slope of  $x_{g2,3}(\varepsilon_{2,3})$  is small the error is large.

The easy agreement of the simulations with the data (and the small error of the  $\varphi(x)$ -reconstructions) allows to state that the key point of the simulations for the detector with floating strips is a response function  $p(x)$  with the form of figure 3. This  $p(x)$  gives even an explanation of the better quality of the reconstruction (and of its error almost independent from  $\theta$ , as it will be seen in the following). In fact, for signal distributions of the size used, its effect is similar to a triangular  $p(x)$  with base  $2\tau$ . As proved in ref. [1], the triangular function with base  $2\tau$  is one of the response function that are free from the COG discretization error for any signal distribution (ideal detector). The noise and the information loss, due to a restricted number of strips used in the algorithm, are the most significant limiting factors in the reconstruction, and a true triangular  $p(x)$  gives modest improvements.

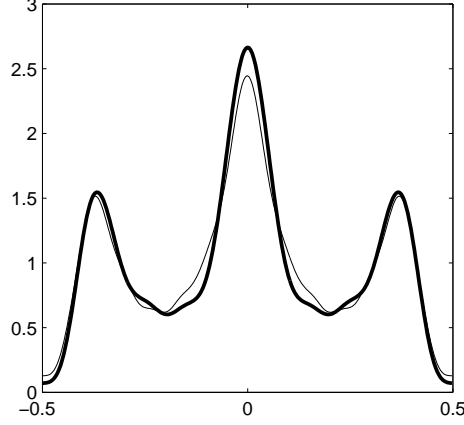


Figure 7: Probability distribution  $\Gamma^p(x_{g3})$  of the simulation (thin line) and of the data (thick line).

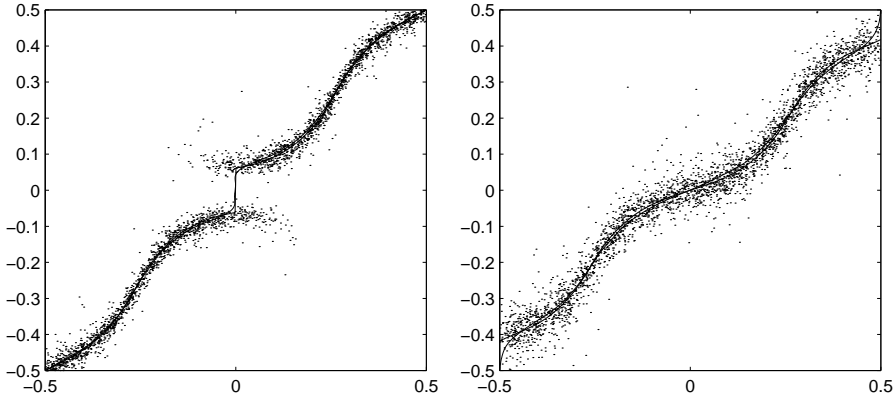


Figure 8: To the left, the  $x_{g2}$ -positions in function of the corresponding  $\epsilon$  for the simulated events. The two overlapping curves are:  $x_{g2}(\epsilon_2)$  and the noiseless  $x_{g2}(\epsilon)$ . To the right,  $x_{g3}$  and  $\epsilon$  for the simulated events. The two overlapping curves are  $x_{g3}(\epsilon_3)$  and the noiseless  $x_{g3}(\epsilon)$ .

## 6 Normal-strip side

### 6.1 The Response Function

The ohmic-side of the sensor has no floating strips, we will call normal strip side the ohmic-side, and normal strips its strips.

The lack of a capacitive coupling in this side produces a large reconstruction error. For  $\theta = 0^\circ$ , an important fraction of the signal tends to concentrate on a single strip giving an high probability to have  $x_{g2,3} \approx 0$ . A small interstrip capacity is present, but its crosstalk effect remains modest. At any rate, to produce a good simulation, we have to account for this crosstalk with the following empirical response function  $p(x)$ :

$$p(x) = \int_{-\infty}^{+\infty} dx' \Pi(x-x') \left\{ 0.91\delta(x') + 0.063[\delta(x' - \tau/2) + \delta(x' + \tau/2)] \right. \\ \left. + 0.027[\delta(x' - 3\tau/2) + \delta(x' + 3\tau/2)] \right\} \quad (23)$$

The main part of  $p(x)$  is given by  $0.91\Pi(x)$  (i.e., an interval function), and the small terms are selected

to produce an uniform crosstalk.  $p(x)$  is fine tuned to produce a good agreement of the histograms (and cross-correlations) obtained from the simulation with the corresponding obtained from the data.

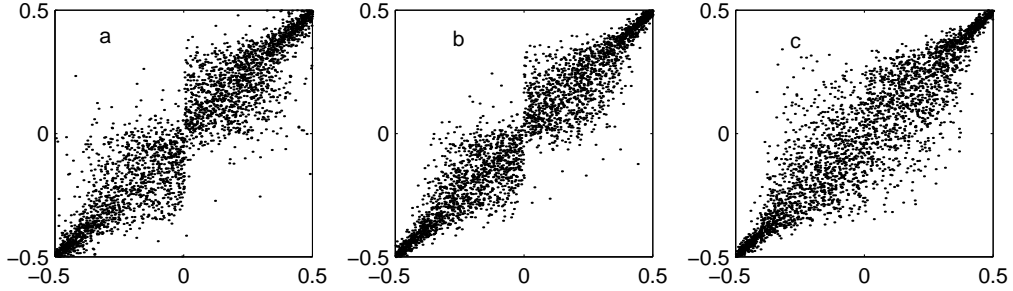


Figure 9: Samples of  $\{\varepsilon_3(x_{g3}(j)), \varepsilon_2(x_{g2}(j))\}$ . Figure a) for the data, b) the simulations with crosstalk, and c) the simulations without the crosstalk.

In figure 9, we show the correlation of  $\varepsilon_3(x_{g3}(j))$  vs.  $\varepsilon_2(x_{g2}(j))$  in the data, in the simulation with the crosstalk of equation 23, and without crosstalk ( $p(x) = \Pi(x)$ ). As it is clearly seen, the absence of crosstalk produces a plot drastically different from the data. The crosstalk of equation 23 gives correlations with exclusion regions very similar to the experimental one. This test looks more sensitive than the histograms, here even the noise model can be compared.

## 6.2 Simulations

The simulated events are generated as in the case of the floating strip, with some evident modifications. The parameter  $\alpha$  is taken to be 0.0289 (partially scaled to keep into account the difference of  $\tau = 67\mu\text{m}$ ), and  $p(x)$  is given by equation 23.

A set of random  $\varepsilon_i$  values is generated with an uniform distribution over three strips. The  $\varepsilon_i$ -values are the COG of initial ionization distributions. The fraction of the charge collected by each strip is calculated with equation 14, and the simulated collected charge is obtained multiplying by a random factor with a distribution similar to that in the data. A fluctuation with a Poisson distribution is added to the charge collected in each strip. The additive noise is gaussian with zero mean and standard deviation similar to the noise distribution of the distant strips in the data. A comparison of the probability distributions for  $x_{g2}$  and  $x_{g3}$  is reported in figure 10. The plots are produced as explained in section 5.4 for the floating strip side. Even in this case the agreement is excellent. Figure 11 is the equivalent of figure 8 for the normal strip side. Here the simulated events are scattered far from the curves  $x_{g2,3}(\varepsilon_{2,3})$  or the noiseless  $x_{g2,3}(\varepsilon)$ , and the position reconstruction with  $\varepsilon_{2,3}(x_{g2,3})$  has a larger error compared to the floating strip side. The overlaps of  $x_{g2,3}(\varepsilon_{2,3})$  with the noiseless  $x_{g2,3}(\varepsilon)$  are smaller than these for the floating strips.

## 7 Directions with $\theta \neq 0$

### 7.1 Simulations

The angle  $\theta$  is defined in figure 1, and  $L_x$  is given by  $L_x = L_0 \tan(\theta)$ . With  $L_x \neq 0$ , the different diffusion times of the top and the bottom of the track are shifted, and  $\varphi(x)$  becomes asymmetric. Figure 2 shows these asymmetries.

For  $\theta \neq 0$  we have no data consistent with these used for  $\theta = 0$ , and we cannot test the simulations. But, given the agreement reached for  $\theta = 0$ , it is reasonable to proceed with our simulations at least

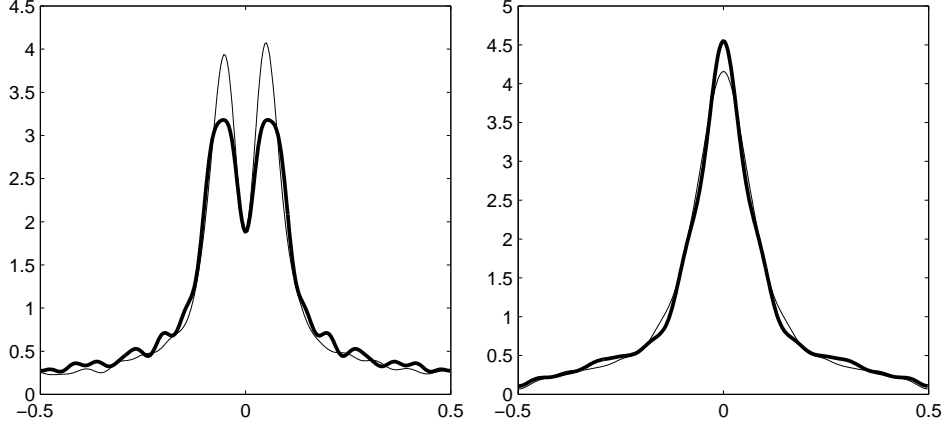


Figure 10: To the left, probability distribution for  $x_{g2}$  from the simulations (thin line), and from the data (thick line). To the right, the probability distribution for  $x_{g3}$ ; simulations (thin line), data (thick line).

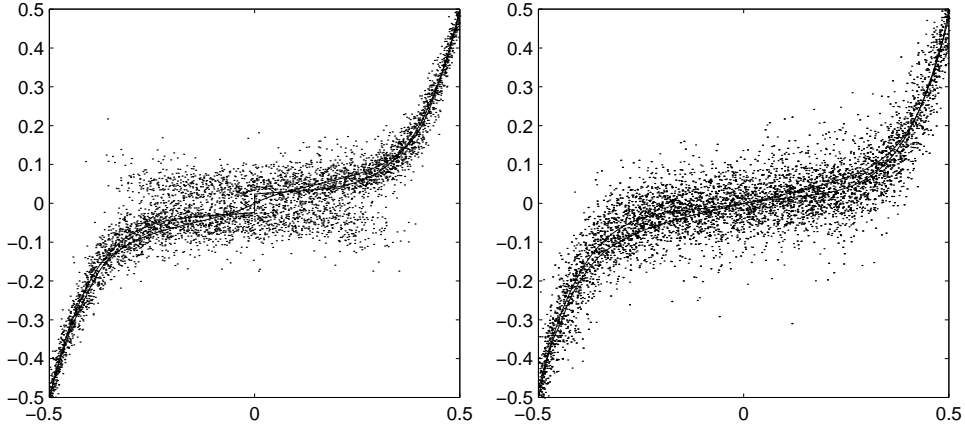


Figure 11: To the left, a sample of  $\{\epsilon(j), x_{g2}(j)\}$ , the two curves are: the discontinuous one is the noiseless  $x_{g2}(\epsilon)$ , the other is  $x_{g2}(\epsilon_2)$  with  $\epsilon_2$  given by equation 20. To the right, a sample of  $\{\epsilon(j), x_{g3}(j)\}$ . The two curves are the noiseless  $x_{g3}(\epsilon)$  and  $x_{g3}(\epsilon_3)$

in the range  $0^\circ \leq \theta \leq 20^\circ$ . At any rate, we will prove with analytical development our critical results delineated by the simulations. The  $\theta$ -range is covered with steps of  $1^\circ$ .

For  $\theta > 20^\circ$ , the loss of information of  $x_{g2}$  and  $x_{g3}$  starts to produce non optimal results. Algorithms with a greater number of strips must be explored and the simulations should be calibrated with the data. Our use of  $x_{g4}$  will be limited to correct the integration constant of equation 20.

In this section  $\epsilon_n$  and  $x_{gn}$  indicate the full reconstructed positions in the absolute reference system of the sensor. The origin of this reference system is in the center of a strip and the positions of the maximum signal strip is always an integer number.

## 7.2 Standard Deviations for the Reconstructions (Normal Strips)

The simulations allow to calculate the standard deviation (SD) in function of  $\theta$  of the various reconstructions, we will start with the normal strips. The trends of the SD can be compared with the COG error for an infinite sampling of noiseless signal distribution. The mean square error for uniform response func-



tion was calculated in ref. [2] for two dimensional systems. The reduction to one dimensional systems is trivial and gives:

$$\int_{-1/2}^{+1/2} (x_g(\varepsilon) - \varepsilon)^2 d\varepsilon = \sum_{k=1}^{+\infty} |\Phi(-2k\pi)|^2 (P'(-2k\pi))^2 \quad (24)$$

Figure 12 reports various plots of SDs. The continuous line is the result of equation 24 at various  $\theta$ . The other curves are the SD of  $\varepsilon_{2,3}(x_{g2,3}) - \varepsilon$  and of  $x_{g2,3} - \varepsilon$ . For small  $\theta$  the line of is not far from that of  $\varepsilon_2(x_{g2}) - \varepsilon$ . For  $\theta > 12^\circ$  the SD of  $x_{g2} - \varepsilon$  starts to increase abandoning the common trends of the other reconstructions. The origin of this increase is connected to the drastic loss of information of the two strip algorithm that produces a large set of forbidden values around  $x_{g2} \approx 0$ . In spite of this, the  $x_{g2}$ -algorithm gives an excellent reconstruction  $\varepsilon_2(x_{g2})$  with a SD better than the SD of  $\varepsilon_3(x_{g3}) - \varepsilon$ .

A sort of saturation effect appears when  $\theta > 12^\circ$  for  $\varepsilon_2(x_{g2}) - \varepsilon$ ,  $\varepsilon_3(x_{g3}) - \varepsilon$  and  $x_{g3} - \varepsilon$ . Part of the trend of the analytical calculation 24 is present in the reconstruction errors up to  $\theta \approx 12^\circ$ , beyond this value the noise (and the loss of information) dominates and the algorithms tend to loose their relations to the noiseless lossless model.

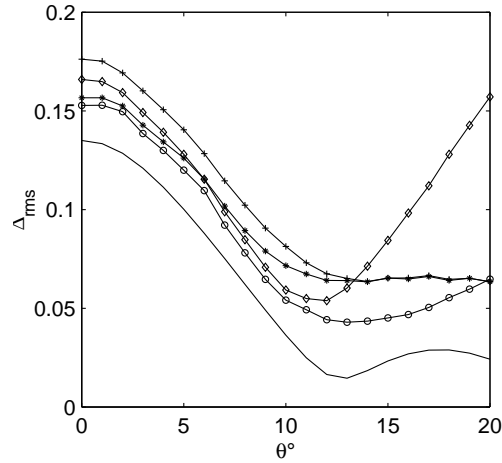


Figure 12: Standard deviations for various reconstructions, diamond  $x_{g2}$ , circle  $\varepsilon_2$ , crosses  $x_{g3}$ , asterisks  $\varepsilon_3$ , continuous line the results of equation 24

### 7.3 Distributions of $\varepsilon_{2,3} - \varepsilon$

The SD's are not good parameters to characterize the differences  $\varepsilon_{2,3}(x_{g2,3}) - \varepsilon$ . Interesting plots are the histograms of the probabilities of  $\varepsilon_{2,3}(x_{g2,3}) - \varepsilon$  and of  $x_{g2,3} - \varepsilon$ . We report them for  $\theta = 0^\circ$  and  $\theta = 5^\circ$  in the figures 13. The differences  $\varepsilon_{2,3}(x_{g2,3}) - \varepsilon$  have distributions similar to the Cauchy probability density with a small full width at half maximum (FWHM). It is interesting the dramatic reduction of the FWHM of  $\varepsilon_{2,3}(x_{g2,3}) - \varepsilon$  respect to the FWHM of  $x_{g2,3} - \varepsilon$  at low  $\theta$ . No comparable reduction is observed in the SDs that, excluding the SD of  $x_{g2} - \varepsilon$ , have values and trends similar. The FWHM is an important parameter to describe these distributions. At increasing  $\theta$ , the distributions slowly tend to gaussians.

### 7.4 Error Due to $\varphi(x)$ Asymmetry

In figure 13 we start to see the effect of the asymmetry of  $\varphi(x)$  in the integration constant of equation 20. For  $\theta = 5^\circ$ , the maximum of the distributions for  $\varepsilon_{2,3}(x_{g2,3}) - \varepsilon$  is shifted from zero, and all the reconstructed values are shifted accordingly. Even if modest in the scale of the SDs, this shift is of the same

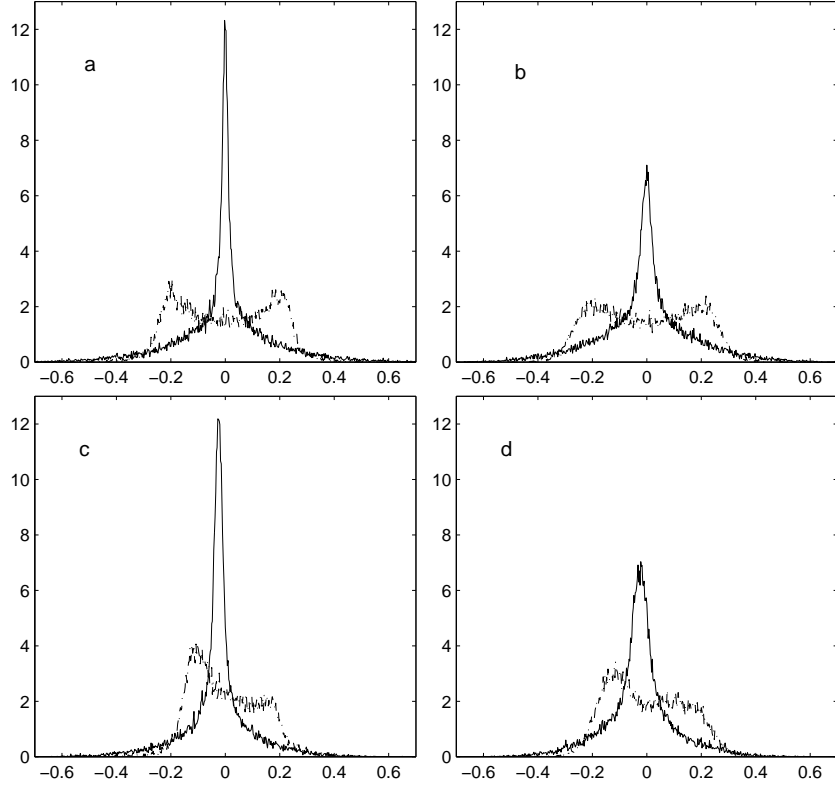


Figure 13: Figure (a) is the histogram of  $\varepsilon_2(x_{g2}) - \varepsilon$  (continuous line) and of  $x_{g2} - \varepsilon$  (dash-dotted line) for normal strips and  $\theta = 0$ . (b) is the histogram of  $\varepsilon_3(x_{g3}) - \varepsilon$  (continuous line) and of  $x_{g3} - \varepsilon$  (dash-dotted line). (c) and (d) are for  $\theta = 5^\circ$ . In (c) it is evident the non zero position of the maximum.

order of the FWHM. For the floating strip sensor, the shift can be of the order of the SD, as we will see in the following.

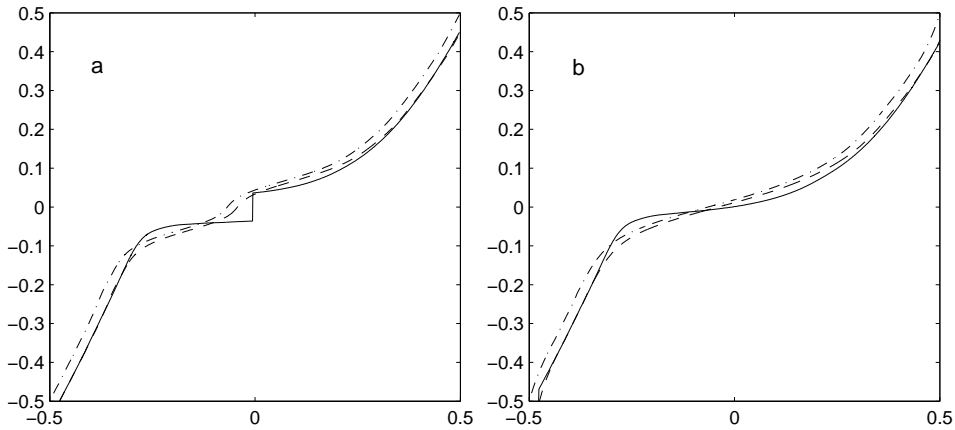


Figure 14: To the left (a) is the plot of  $x_{g2}$  vs  $\varepsilon_2(x_{g2})$  (dash-dot line) and  $x_{g2}$  noiseless vs.  $\varepsilon$  (solid line) for  $\theta = 5^\circ$ , the two curves do not coincide as in figure 8, the dashed line is  $x_{g2}$  vs  $\varepsilon_2^r(x_{g2})$  corrected as explained in the following. This curve has large overlaps with the noiseless one. To the right (b) the plots of  $x_{g3}$  versus  $\varepsilon_3(x_{g3})$  (dash dot line) and of  $x_{g3}$  noiseless versus  $\varepsilon$  (solid line) and  $x_{g3}$  vs  $\varepsilon_3^r(x_{g3})$  (dashed line)

Figure 14 illustrates the origin of the shift in the maximum of the  $\varepsilon_{2,3}(x_{g2,3}) - \varepsilon$  probabilities. The lines  $x_{g2,3}(\varepsilon_{2,3})$  do not overlap with the noiseless  $x_{g2,3}(\varepsilon)$ , as we have for  $\theta = 0$ , they are shifted to right by a small quantity, thus the reconstructed values  $\varepsilon_{2,3}(x_{g2,3})$  of the events, the maximum and the mean values of  $\varepsilon_{2,3}(x_{g2,3}) - \varepsilon$ . The corrections, we are going to define, will regenerate the overlaps. Having to work with mean values, definitions are necessary:

$$M\varepsilon_{2,3} = \sum_{j=1}^N \frac{\varepsilon_{2,3}(x_{g2,3}(j)) - \varepsilon(j)}{N} \quad (25)$$

$$M_{x2,3,4}^l = \sum_{j=1}^N \frac{x_{g2,3,4}(j) - \mu(j)}{N},$$

where  $\mu(j)$  is the position of the center of the strip with the maximum signal for the event  $j$ . The term  $x_{gn}(j) - \mu(j)$  is the COG of the event  $j$  in the virtual strip we used to calculate the probability distribution. We call local these averages to stress their independence from the true event position.

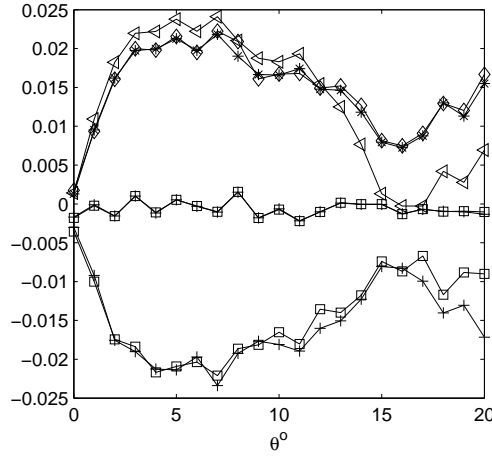


Figure 15: Plots of mean values in function of  $\theta$ . Diamonds  $M_{x4}^l$ , asterisks  $M_{x3}^l$ , triangles  $M_{x2}^l$ , crosses  $M\varepsilon_2$ , squares  $M\varepsilon_3$ , the lines around zero are  $M\varepsilon_2^l$  and  $M\varepsilon_3^l$

Figure 15 summarizes the  $\theta$ -dependent averages:  $M\varepsilon_2$ ,  $M\varepsilon_3$ ,  $M_{x2}^l$ ,  $M_{x3}^l$  and  $M_{x4}^l$ . The figure is complex to read in detail. But, at first glance, two almost symmetric group of lines respect to zero are evident. The lines for negative values are the systematic errors  $M\varepsilon_2$  and  $M\varepsilon_3$ . The lines for positive values are the averages  $M_{x2}^l$ ,  $M_{x3}^l$  and  $M_{x4}^l$ . The lines (overlapped) around zero are the corrected  $M\varepsilon_2$  and  $M\varepsilon_3$ . It easy to guess that the sought corrections are near to  $M_{x2}^l$ ,  $M_{x3}^l$  or  $M_{x4}^l$ , in fact, the sum of  $M\varepsilon_2$  or  $M\varepsilon_3$  with  $M_{x3}^l$  or  $M_{x4}^l$  is around zero. A careful observation shows that  $M_{x2}^l$  is not a good correction.

Given these empirical evidences, it is important to demonstrate their origin to assure us that no simulation inconsistencies mimic the rule. With this aim, we must go in depth in the reconstruction algorithms to isolate the constants (in average) they contain.

## 7.5 The Complete $\varphi(x)$ -Reconstruction Theorem

First of all, we must demonstrate the last element required to complete the reconstruction theorem that evidently emerges from equations 15 and 20. The steps of this reconstruction are recalled here.

Given a set of noiseless and lossless events, originating by the same  $\varphi(\varepsilon)$ , the COG  $x_g$  (infinite sampling) for each event is calculated and a probability distribution  $\Gamma(x_g)$  is obtained.

The events are supposed to uniformly illuminate all the strips, and a periodic  $\Gamma^p(x_g)$  ( $\Gamma^p(x_g) = \Gamma^p(x_g + L) \forall L \in \mathbb{Z}$ ) is generated.

The integration of  $\Gamma^p(x_g)$  gives:

$$\varepsilon(x_g) = \int_{x_g^0}^{x_g} \Gamma^p(y) dy + \varepsilon(x_g^0). \quad (26)$$

Equation 26 produces the functions  $\varepsilon(x_g)$  or  $x_g(\varepsilon)$ . The periodicity of  $\Gamma^p(x_g)$  allows the form 21 of a FS for their differences with the following expressions for  $\alpha_n$  and  $\beta_k$ :

$$\begin{aligned} \alpha_n &= \int_{-1/2}^{+1/2} e^{-i2\pi ny} (\varepsilon(y) - y) dy \\ \beta_k &= \int_{-1/2}^{+1/2} (y - \varepsilon(y)) e^{-i2\pi k \varepsilon(y)} \Gamma(y) dy \end{aligned} \quad (27)$$

For a normalized non negative  $\varphi(\varepsilon)$  ( $\varphi(\varepsilon) = \Pi(\varepsilon) \varphi(\varepsilon)$ ) and the response function  $p(x) = \Pi(x)$ , the derivate  $dx_g(\varepsilon)/d\varepsilon$  allows the selection of the function  $\varphi(\varepsilon - 1/2)$ :

$$\Pi(\varepsilon - 1/2) \frac{dx_g}{d\varepsilon} = \varphi(\varepsilon - 1/2). \quad (28)$$

The limitation of the function  $\varphi(\varepsilon)$  to have the support less than a strip can be easily overcome given  $p(x) = \Pi(x)$ . Assembling various strips the support can be extended. This method cannot be used with the response function used in equation 18. Even in this case the function  $\varphi(\varepsilon)$  can be reconstructed, but its support must be less than half strip.

The equations 26 and 28 contain the integration constant  $\varepsilon(-1/2)$ . In the simulations,  $\varepsilon(-1/2)$  is always set equal to  $-1/2$ , this position is exact for symmetric  $\varphi(\varepsilon)$ . For asymmetric  $\varphi(\varepsilon)$  the incorrect  $\varepsilon(-1/2)$  shifts  $\varphi(\varepsilon)$  by  $\varepsilon(-1/2) + 1/2$  giving an incorrect reconstruction. The exact value  $\varepsilon(-1/2)$  must be extracted from the data to extend the reconstruction theorem to asymmetrical  $\varphi(\varepsilon)$ .

Identical reasoning can be applied to the conventional  $\eta$  algorithm, here the integration starts from zero, the position  $\varepsilon(0) = 0$  is correct for  $\theta = 0$  and symmetric  $\varphi(\varepsilon)$ . For  $\theta \neq 0$  a non zero constant is required.

The empirical property, evident in figure 15, gives a track to complete the theorem. Due to our definitions, we can write the following relations for the mean value of  $x_g$ :

$$\int_{-1/2}^{+1/2} \Gamma^p(x_g) x_g dx_g = \int_{-1/2}^{+1/2} x_g \frac{d\varepsilon(x_g)}{dx_g} dx_g = \int_{\varepsilon(-1/2)}^{\varepsilon(+1/2)} x_g(\varepsilon) d\varepsilon \quad (29)$$

Our assumption about the reconstruction of noiseless and lossless events gives for  $x_g(\varepsilon)$  the equation:

$$x_g(\varepsilon) = \varepsilon + i \sum_{k \neq 0, k = -\infty}^{+\infty} \Phi(-2k\pi) P'(-2k\pi) \exp(i2k\pi\varepsilon) \quad (30)$$

for a generic uniform and symmetric response function  $p(x)$ , and any normalized  $\varphi(\varepsilon)$ . For non symmetric  $p(x)$  a constant term must be added.

A fundamental property of equation 30 is the absence of the  $k = 0$ -term in the sum of exponentials (FS). The integral of  $x_g(\varepsilon)$  on a strip length (the period of the FS) has no contribution from the FS, and equation 29 becomes:

$$\int_{\varepsilon(-1/2)}^{\varepsilon(+1/2)} x_g(\varepsilon) d\varepsilon = \frac{1}{2} [\varepsilon(1/2)^2 - \varepsilon(-1/2)^2] \quad (31)$$

From the periodicity of  $x_g(\varepsilon) - \varepsilon$  and  $\varepsilon(x_g) - x_g$  it follows:

$$\varepsilon(x_g) - x_g = \varepsilon(x_g - 1) - (x_g - 1) \quad \varepsilon(1/2) - 1/2 = \varepsilon(-1/2) + 1/2 = \Delta_{1/2}$$

Equation 29 can be finally expressed as:

$$\int_{-1/2}^{+1/2} \Gamma^p(x_g) x_g dx_g = \Delta_{1/2} = \varepsilon(-1/2) + 1/2. \quad (32)$$

$\Delta_{1/2}$  is just the missing part of the integration constant of equation 26 that completes our initial guess of  $\varepsilon(-1/2) = -1/2$ . To conclude,  $\Gamma^p(x_g)$  and its mean value on a strip length allow the reconstruction of asymmetric  $\varphi(\varepsilon)$ .

Excluding equation 28, all the other equations of this section are more general than the needs of  $\varphi(\varepsilon)$ -reconstruction, and they will be used to correct the systematic error due to the asymmetry in our noisy case.

## 7.6 Correction of the Systematic Error

As we can see in figure 15, the systematic error is the same for both algorithms. This is not unexpected. In noiseless case,  $x_{g2,3} = \pm 1/2$  is given by the same  $\varepsilon$ -value. If the noise does not contribute in average (and here this is the case for our acceptance of all the energy values corrupted by the noise), the missing constant  $\varepsilon(x_{g2,3} = -1/2) + 1/2$  is the same for  $M_{\varepsilon 2}$  and  $M_{\varepsilon 3}$ .

A more precise strategy for the correction of  $\varepsilon_{2,3}$  can be found studying their common forms. The final position  $\varepsilon_{2,3}(j)$  of the event  $j$  is given by:

$$\varepsilon_{2,3}(j) = x_{g2,3}(j) + \sum_{k=-L}^L \alpha_k(2,3) e^{i2\pi k x_{g2,3}(j)} \quad (33)$$

where  $x_{g2,3}(j)$  is the COG of the event  $j$  in their true positions (more or less near to the maximum signal strip of the event  $j$ ).  $\{\alpha_l(2,3)\}$  are the constants of the FS for  $\varepsilon_{2,3}$ . We need the average of  $\varepsilon_{2,3}(j) - \varepsilon(j)$ , the averages of  $\varepsilon_{2,3}(j)$  and  $x_{g2,3}(j)$  are transparent. Due to the non uniform distribution of  $x_{gn}$  in the exponents, the average of the FS is more complex. The  $x_{gn}(j)$  are in the global reference system, but the shift of the integer  $\mu(j)$  does not modify the exponentials. The average over  $\Gamma(x_{gn})$  due to the periodicity of the exponentials gives:

$$\int_{-\infty}^{+\infty} \Gamma(x_{gn}) e^{i2\pi k x_{gn}} dx_{gn} = \int_{-1/2}^{+1/2} \Gamma^p(x_{gn}) e^{i2\pi k x_{gn}} dx_{gn}, \quad (34)$$

but for equations 19 and 22 the average of the FS becomes:

$$\sum_{k=-L}^{+L} \alpha_k \int_{-1/2}^{+1/2} \Gamma^p(x_{gn}) e^{i2\pi k x_{gn}} dx_{gn} = \alpha_0 + \sum_{k=-L}^{+L} \alpha_k \alpha_{-k} i 2\pi k. \quad (35)$$

The bilinear term in  $\alpha_k$  is zero due to the  $k$ -antisymmetry of its elements, and the average  $M\varepsilon_{2,3}$  is:

$$M\varepsilon_{2,3} = \alpha_0(2,3) + \sum_{j=1}^N \frac{x_{g2,3}(j) - \varepsilon(j)}{N} = \alpha_0(2,3) + M_{x_{2,3}}^l + \sum_{j=1}^N \frac{\mu(j) - \varepsilon(j)}{N} \quad (36)$$

Recalling the form 27 of  $\alpha_0$  for any algorithm, the integration on a triangle gives:

$$\alpha_0 = \int_{-1/2}^{+1/2} dy \left[ \int_{-1/2}^y dy' \Gamma^p(y') - y \right] - \frac{1}{2} = - \int_{-1/2}^{1/2} dy' \Gamma^p(y') y' \quad (37)$$

In the simulations (and in the data)  $\alpha_l$ ,  $M_{x_{2,3}}^l$  and  $M\varepsilon_{2,3}$  are stochastic variables fluctuating around their mean values, and the following equalities can experience fluctuations due to the statistics:

$$\alpha_0(2,3) = -M_{x_{2,3}}^l \quad \Rightarrow \quad M\varepsilon_{2,3} = \sum_{j=1}^N \frac{\mu(j) - \varepsilon(j)}{N} \quad (38)$$

Any reference to the used algorithm disappears in the expression of  $M\mathcal{E}_{2,3}$  and  $M\mathcal{E}_2 \approx M\mathcal{E}_3$ . The relation  $\alpha_0(2,3) = -M_{x_{2,3}}^l$  must be handled with care. Different probability distributions are present in the two sides:  $\alpha_0(2,3)$  is defined on a period of the periodic  $\Gamma^p(x_{g2,3})$ ,  $M_{x_{2,3}}^l$  is defined on  $\Gamma(x_{g2,3})$ . These differences are negligible in our simulations of  $x_{g2,3}$ , but for  $x_{g4}$  it is large and the systematic error of  $\mathcal{E}_4$  is different from that of  $\mathcal{E}_{2,3}$ .

The correction of  $M\mathcal{E}_{2,3}$  is obtained recalling equation 30, that for an infinite sampling gives (for asymmetric  $p(x)$  the following integral is equal to the shift of the COG of  $p(x)$  respect to the strip center) :

$$\int_{-1/2}^{1/2} (x_g(\varepsilon) - \varepsilon) d\varepsilon = 0 \Rightarrow \frac{1}{N} \sum_{j=1}^N x_{gn}(j) - \varepsilon(j) = 0 \quad (39)$$

where  $x_{gn}(j)$  approximate an infinite sampling containing all the signal strips in the event. For  $\theta \leq 20^\circ$ ,  $x_{g4}$  is negligibly different from an infinite sampling and equation 39 can be recast:

$$\sum_{j=1}^N \frac{x_{g4}(j) - \mu(j)}{N} + \sum_{j=1}^N \frac{\mu(j) - \varepsilon(j)}{N} = 0 \rightarrow M_{x4}^l = - \sum_{j=1}^N \frac{\mu(j) - \varepsilon(j)}{N}. \quad (40)$$

The required correction is the mean value of  $x_{g4}(j)$  in the reference system of the maximum signal strip we used to collect all the events (in principle scattered in all the detector).

In figure 15, we see that even  $M_{x3}^l$  can be a good correction in many cases.

We pointed out a possible small non zero value of  $M_{x_{2,3}}^l + \alpha_0(2,3)$ , for this the complete correction strategy is expressed by the following rule (for the algorithms with two and three strips):

$$\mathcal{E}_{2,3}^r(j) = \mathcal{E}_{2,3}(j) - M_{x_{2,3}}^l - \alpha_0(2,3) + M_{x4}^l. \quad (41)$$

For  $\mathcal{E}_4(j)$  the correction reduces to the subtraction of  $\alpha_0(4) = -\Delta_{1/2}$  as imposed by equation 32 for the infinite sampling .

In figure 14, the dashed lines is obtained shifting  $\mathcal{E}_{2,3}(x_{g2,3})$  by  $-M_{x_{2,3}}^l - \alpha_0(2,3) + M_{x4}^l$  and the new lines have a better overlap with the noiseless  $x_{g2,3}(\varepsilon)$ .

Equation 41 is able to correct algorithms where  $\alpha_0(2,3)$  is widely different from  $M_{x_{2,3}}^l$  as in our application of an aspect of the  $\eta$ -algorithm. In the  $\eta$ -algorithm, the  $\eta$ -values are  $0 \leq \eta \leq 1$ , and the integration on  $\Gamma(\eta)$  start from zero. For symmetric  $\varphi(x)$ , zero is the right integration constant of equation 26, we use this zero constant for  $\mathcal{E}_{2,3}$  at all  $\theta \leq 20^\circ$ . In figure 16, the systematic error of  $M\mathcal{E}_{2,3}$  is reported.

Even here  $M\mathcal{E}_2(\theta)$  and  $M\mathcal{E}_3(\theta)$  are overlapping. An explanation of this can be obtained observing that  $x_{g2} = 0$  and  $x_{g3} = 0$  are obtained (in average) for the same  $\varepsilon$ -value, the constant required to correct the systematic error. The differences of  $\alpha_0(2,3)$  from  $-M_{x_{2,3}}^l$  can be seen by the lowest lines of figure 16, these are  $M\mathcal{E}_{2,3} - \alpha_0(2,3) - M_{x_{2,3}}^l$  and are widely different from  $M\mathcal{E}_{2,3}$ . In this case, the systematic error is larger than the case with the integration starting at  $-1/2$ .

The overlap of  $M\mathcal{E}_2(\theta)$  with  $M\mathcal{E}_3(\theta)$  is a special property of the points  $\varepsilon(-1/2)$  and of  $\varepsilon(0)$ , it disappears with a different stating point of the  $\Gamma^p(x_g)$ -integration.

## 7.7 SD for the Floating Strip Side

For  $\theta = 0^\circ$  the SD's of the various reconstructions are smaller than that of normal strips. At increasing  $\theta$ , the error is almost constant showing that the noise is the dominant factor in reducing the resolution. The SD of  $x_{g2} - \varepsilon$  starts to increase for  $\theta > 5^\circ$ , the loss of information creates a large gap in the  $x_{g2}$ -values around  $x_{g2} = 0$ . The reconstruction  $\mathcal{E}_2$  is able to keep the error low, but after  $15^\circ$  the SD of  $\mathcal{E}_3 - \varepsilon$  is the lowest. The infinite sampling noiseless  $x_g$ -error curve (of equation 24) is always lower than all the other,

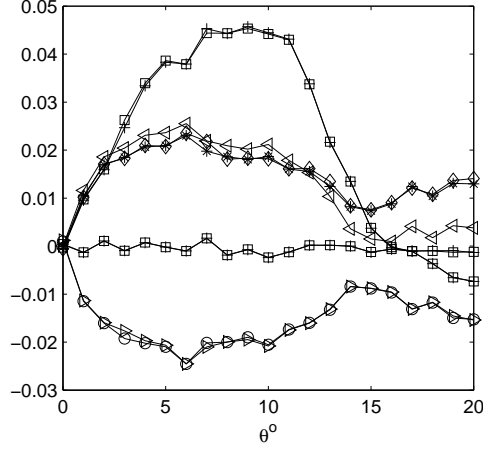


Figure 16: Plots of mean values in function of  $\theta$ . Crosses  $M\epsilon_2$ , squares  $M\epsilon_3$ , diamonds  $M^l_{x4}$ , asterisks  $M^l_{x3}$ , triangles  $M^l_{x2}$ . The lines around zero are  $M\epsilon_2^r$  and  $M\epsilon_3^r$ .

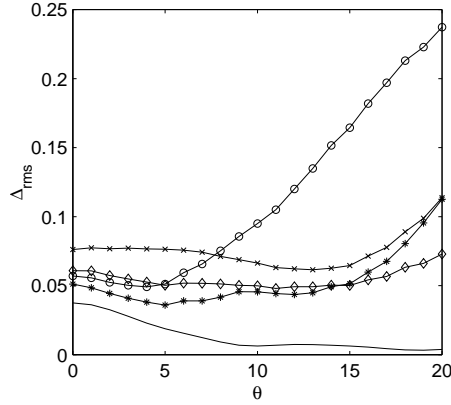


Figure 17: Trends of the rms errors for various reconstruction algorithms with  $\theta^\circ$ : crosses  $x_{g3} - \epsilon$ , circles  $x_{g2} - \epsilon$ , diamonds  $\epsilon_3 - \epsilon$ , asterisks  $\epsilon_2 - \epsilon$ , continuous infinite sampling analytical calculation

as we saw in the case of normal strips. The SD of  $\epsilon_{2,3}$  and  $x_{g3}$  show an almost saturating trend up to  $15^\circ$  and after they start to increase.

## 7.8 Distributions of $\epsilon_{2,3} - \epsilon$

As for the normal strip sensors, the SD (or the rms-error) is not the best parameter to describe the distributions of the differences  $\epsilon_{2,3} - \epsilon$ . Even for the floating strip sensor, the distributions of the difference  $\epsilon_{2,3} - \epsilon$  have some similarities with a Cauchy distribution. The histograms of  $x_{g2,3} - \epsilon$  are similar to those of  $\epsilon_{2,3} - \epsilon$ . This is due to the response function that approximates an ideal detector for signal distributions of this size.

At increasing  $\theta$  a systematic shift of the reconstructed  $x_{g2,3}(\epsilon_{2,3})$  respect to the noiseless ones is present in figure 19. A shift is evident even in the histograms of the differences  $\epsilon_{2,3} - \epsilon$ .

At increasing  $\theta$ , figures 18c and d and figure 19 show shifts similar to those discussed above for the normal strips, and their origin is identical. As anticipated, their order of magnitude is that of the SD.

The histograms of  $x_{g2,3} - \epsilon$  do not show shifts of the mean values, but small shifts are present. The

mean value of  $x_g - \varepsilon$  is zero only for the infinite sampling case that is well represented by  $x_{g4}$  for  $\theta \leq 20^\circ$ . In the algorithms with the suppression of signal strips the mean value of  $x_{gn} - \varepsilon$  has a non zero value that can be corrected along the lines of equation 39 and 40.

The corrections of  $M\varepsilon_{2,3}$  are in the form of equation 41. In this sensor side we detected a small signal loss for events around the floating strip, but the corrections work well even here as it can be seen in figure 19. Figure 20 reports  $M\varepsilon_{2,3}(\theta)$  and  $M_{x_{2,3,4}}^l(\theta)$ , the overlap of  $M\varepsilon_2(\theta)$  with  $M\varepsilon_3(\theta)$  indicates that an identical correction is needed and  $M_{x4}^l$  is the correction. The approximate identity  $\alpha_0(2,3) = M_{x_{2,3}}^l$  here is well verified.

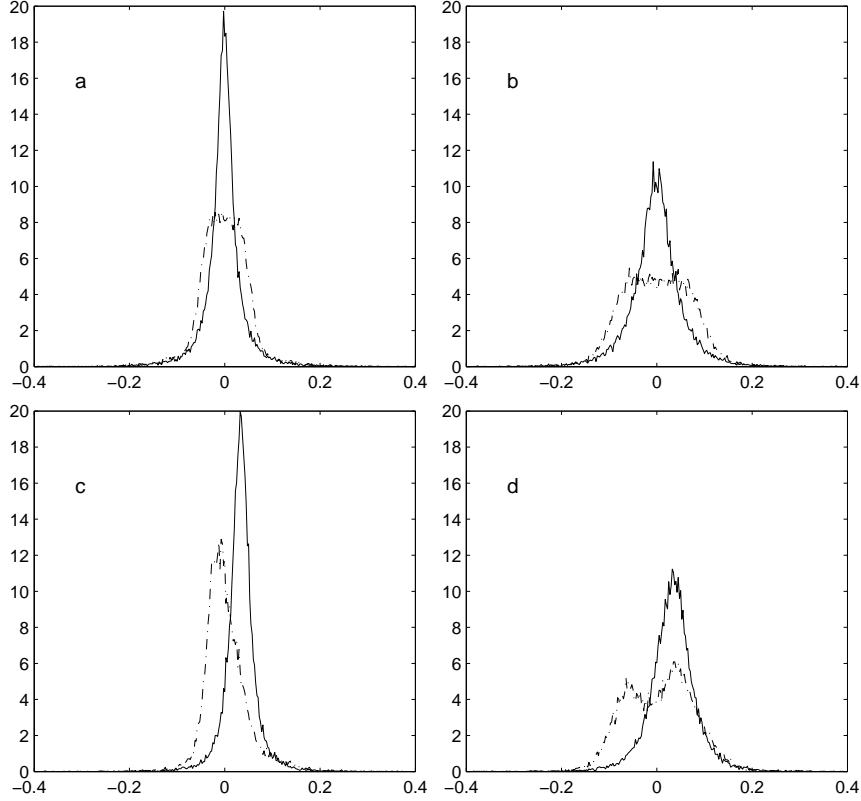


Figure 18: To the left (a) it is the histogram of  $\varepsilon_2(x_{g2}) - \varepsilon$  (continuous line) and of  $x_{g2} - \varepsilon$  (dash-dotted line) for normal strips and  $\theta = 0^\circ$ . To the right (b) the histogram of  $\varepsilon_3(x_{g3}) - \varepsilon$  (continuous line) and of  $x_{g3} - \varepsilon$  (dash-dotted line). c) and d) are for  $\theta = 3^\circ$ . Here, a shift of the maximum respect to zero is evident.

## 8 Conclusions

The simulations we realized show useful applications of the results of ref. [1]. It turns out sufficiently easy to extract free parameters from the data. The response functions of the strips are optimized for floating strip sensors and normal sensors. For floating strip sensors and signal distributions of this size, the obtained response function can be considered a rough approximation of triangular function with base  $2\tau$ . This explains the better quality of the position reconstructions of these detectors. The triangular response function (with base  $2\tau$ ) is the simplest response form of a detector (defined ideal in ref [1]) where the COG of the hit strips is the exact reconstruction algorithm. The simulations of non orthogonal incoming directions (and asymmetric signals) have immediately underlined the existence of a systematic error in the standard applications of the  $\eta$  algorithm. From the form of our equations, the existence



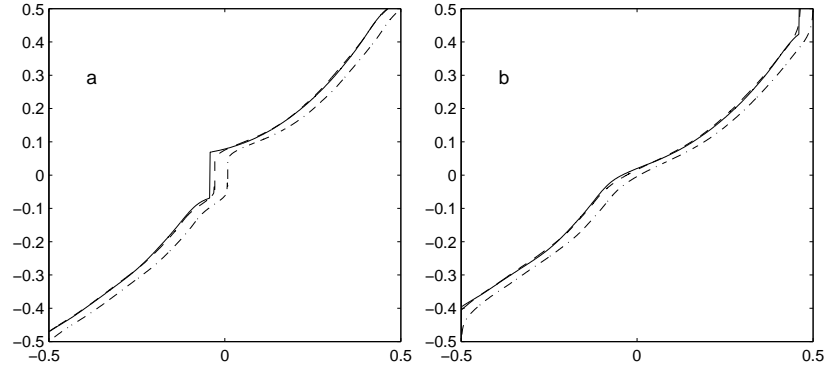


Figure 19: To the left (a) is the plot of  $x_{g2}$  vs  $\epsilon_2(x_{g2})$  (dash-dot line) and  $x_{g2}$  noiseless vs.  $\epsilon$  (solid line) for  $\theta = 3^\circ$ , the two curves do not coincide as in figure 8, the dashed line is  $x_{g2}$  vs  $\epsilon_2^r(x_{g2})$  corrected as explained. This curve has large overlaps with the noiseless one. To the right (b) the plots of  $x_{g3}$  versus  $\epsilon_3(x_{g3})$  (dash-dot line) and of  $x_{g3}$  noiseless versus  $\epsilon$  (solid line) and  $x_{g3}$  vs  $\epsilon_3^r(x_{g3})$  (dashed line)

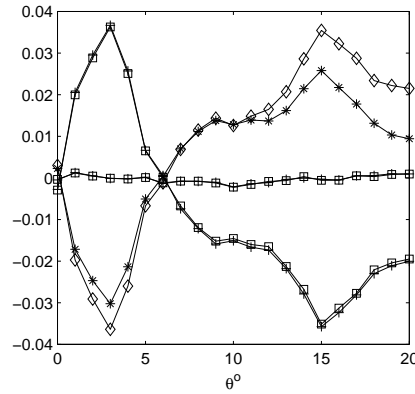


Figure 20: Mean values in function of  $\theta$ , diamonds  $M_{x_4}^l$ , asterisks  $M_{x_2}^l$ , squares  $M\epsilon_3$ , crosses  $M\epsilon_2$ , the lines around zero are  $M\epsilon_3^c$  e  $M\epsilon_2^c$ .

of this type of systematic error is evident from the beginning. The simulations estimate its amplitude, and they give some hint for its suppression. As in the  $\eta$  algorithm, the corrections are extracted from the data. A fundamental step to demonstrate the form of the corrections is the completion of a signal reconstruction theorem for an irregularly sampled, non negative, asymmetric and duration limited signal.

## References

- [1] G. Landi, Nucl. Instr. and Meth. A 485 (2002) 698.
- [2] G. Landi, Nucl. Instr. and Meth. A 497 (2003) 511.
- [3] G. Batignani et al., Nucl. Instr. and Meth. A 277 (1989) 147.
- [4] Acciarri et al., Nucl. Instr. and Meth. A 351 (1994) 300.
- [5] E. Belau et al., Nucl. Instrum. and Meth. A 214 (1983) 253.
- [6] R.N. Bracewell, "The Fourier Transform and Its Application" (McGraw-Hill, New York, NY, 1986).

- [7] D.C. Champeney, "A Handbook of Fourier Theorems" (Cambridge University Press, Cambridge, UK, 1987).
- [8] I. Abt et al., Nucl. Instrum. and Meth. A 423 (1999) 303.
- [9] The PAMELA Collaboration in Proceedings XXVI ICRC Salt Lake City Volume OG.4.2.04 1999
- [10] M. Krammer, H. Pernegger, Nucl. Instr. and Meth. A 397 (1997) 232.